

Understanding the Structural and Electronic Properties of Bismuth Trihalides and Related Compounds

Zeyu Deng, Fengxia Wei, Yue Wu, Ram Seshadri, Anthony K. Cheetham, and Pieremanuele Canepa*



Cite This: <https://dx.doi.org/10.1021/acs.inorgchem.9b03214>



Read Online

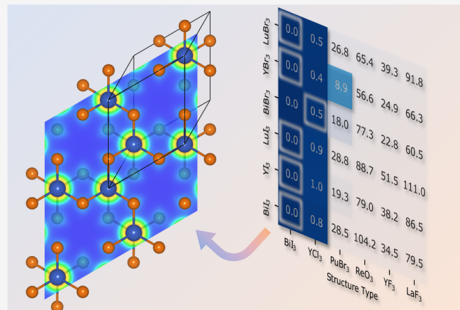
ACCESS |

Metrics & More

Article Recommendations

Supporting Information

ABSTRACT: Bismuth trihalides, BiX_3 ($X = \text{F}, \text{Cl}, \text{Br}$, and I), have been thrust into prominence recently because of their close chemical relationship to the halide perovskites of lead, which exhibit remarkable performance as active layers in photovoltaic cells and other optoelectronic devices. In the present work, we have used calculations based on density functional theory to explore the energetics and electronic properties of BiX_3 in a variety of known and hypothetical structure types. The results for BiX_3 are compared with those obtained for the halides of the later rare earths, represented by YX_3 and LuX_3 . The relative thermodynamic stabilities of the known and hypothetical structures are calculated, along with their band gaps. For the BiX_3 systems, we have explored the role of lone-pair effects associated with bismuth(III), and for BiI_3 , we have compared the predicted structural behavior as a function of pressure with the available experimental data. We have also attempted to synthesize LuF_3 in the perovskite-related ReO_3 -type structure, which is predicted to be only $\sim 7.7 \text{ kJ mol}^{-1}$ above the convex hull. This attempt was unsuccessful but led to the discovery of a new hydrated phase, $(\text{H}_3\text{O})\text{Lu}_3\text{F}_{10}\text{H}_2\text{O}$, which is isomorphous with the known ytterbium analogue.



INTRODUCTION

Metal halide materials possess a rich variety of interesting properties that have resulted in a number of technologically important applications, including their use as scintillator materials for X-ray detection,¹ ionic conductors for energy-storage applications,^{2,3} and their adoption as photoluminescent materials for bioimaging through up-conversion.^{4,5} Recently, hybrid perovskite halides of the general formula $\text{A}^{\text{I}}\text{Pb}^{\text{II}}\text{X}_3$ [A = amine cation, such as CH_3NH_3^+ or $\text{CH}(\text{NH}_2)_2^+$, and $\text{X} = \text{Cl}, \text{Br}$, and I] have attracted significant interest in relation to photovoltaic (PV) and photoluminescence (PL) applications because of their excellent optoelectronic properties, facile synthesis, and low cost.^{6–10} However, the toxicity of lead (Pb) and the sensitivity to moisture of these perovskites have stimulated efforts to find alternative materials that can provide similar or even superior optoelectronic properties without toxicity and stability issues. One strategy involves replacing the divalent metal (Pb^{2+}) with a mixture of monovalent M^{I} and trivalent M^{III} cations to form halide double perovskites of the general formula $\text{A}_2\text{M}^{\text{I}}\text{M}^{\text{III}}\text{X}_6$ (A = alkali metal or amine cation),^{11–16} and thus expands the structural diversity of the family of these perovskite materials. Most of the work in this area has focused on the use of bismuth (Bi) as the M^{III} cation, although there has also been work involving antimony (Sb), as well as rare-earth elements for possible optical and magnetic applications.¹⁸ Another strategy is to use the bismuth halides themselves, especially BiI_3 , which is attracting attention for PV cell applications.^{19,20} However, the low dimensionality of the layered structure adopted by BiI_3 leads to a wider band gap

($\sim 1.8 \text{ eV}$)²¹ compared with the Pb-containing perovskite iodides; hence, it is not ideal for PV applications. One approach to solve this problem would be to identify accessible polymorphs of the bismuth halides that retain a 3D network architecture and should therefore have narrower band gaps. For example, the most obvious structural candidate would be the ReO_3 -type structure,^{22,23} which has a perovskite architecture with no cation in the cavity (i.e., MX_3).

In this paper, we address the question, can we favorably access bismuth halides in 3D structures, such as the ReO_3 type? It is already known that $\text{M}^{\text{III}}\text{F}_3$ compounds, such as ScF_3 and InF_3 , adopt the ReO_3 structure, so this is a reasonable hypothesis. However, BiF_3 and BiCl_3 normally adopt 3D structures related to that of YF_3 and the smaller rare-earth fluorides (Sm–Lu), while BiBr_3 and BiI_3 both have layered structures that are also seen for the rare-earth chlorides (Dy–Lu), bromides, and iodides (Sm–Lu).²⁴ We have therefore used a computational approach to map the thermodynamic stability of the binary trihalides, MX_3 , with $\text{M} = \text{Bi}, \text{Y}$, and Lu and $\text{X} = \text{F}, \text{Cl}, \text{Br}$, and I . This strategy has been applied for several structure types, specifically those of BiI_3 (2D), YCl_3 (2D), PuBr_3 (2D), ReO_3 (3D), YF_3 (3D), and LaF_3 (3D). We have carried out calculations using density functional theory

Special Issue: Bismuth - The Magic Element

Received: November 1, 2019

(DFT) to determine the thermodynamic properties of each of the MX_3 phases in the different structure types. Furthermore, we have performed simulations with hybrid functionals to assess the optoelectronic properties of a subset of relevant materials to identify novel candidates light absorbers and scintillators. We have also assessed the role of electron lone pairs on bismuth by comparing the results for the BiX_3 systems with those for the rare-earth analogues, YX_3 and LuX_3 .

Our computational analysis suggests that although LuF_3 appears to be metastable in the ReO_3 prototype, it should be accessible through synthetic strategies. We explored the synthesis of this phase in the laboratory through a solution evaporation method and found a hydrated phase, $(\text{H}_3\text{O})\text{-Lu}_3\text{F}_{10}\cdot\text{H}_2\text{O}$, crystallizing in the space group $Fd\bar{3}m$, which has not been reported previously.

METHODOLOGY

To assess the thermodynamics of binary trihalides MX_3 with $\text{M} = \text{Lu}, \text{Y}$, and Bi and $\text{X} = \text{F}, \text{Cl}, \text{Br}$, and I using first-principles calculations, we computed the total energies of each compound and calculated the formation energies from their elemental constituents. The formation energies (E_f) were calculated as $E_f = E(\text{M}_y\text{X}_{4-y}) - yE(\text{M}) - (4-y)E(\text{X})$ ($y = 1$), where $E(\text{M}_y\text{X}_{4-y})$, $E(\text{M})$, and $E(\text{X})$ are the DFT total energies for the MX_3 compound, M metal, and X halides, respectively. $E(\text{X})$ is the DFT total energy of element X in its most stable form. For $\text{X} = \text{F}$ and Cl , $E(\text{F}) = E[\text{F}_2(\text{g})]/2$ or $E[\text{Cl}_2(\text{g})]/2$, where $E[\text{F}_2(\text{g})]$ and $E[\text{Cl}_2(\text{g})]$ were calculated on the solid phases of F_2 , Cl_2 , Br_2 , and I_2 , respectively. We only focus on total energies neglecting entropy contributions, pV , and zero-point energies because these are expected to be almost identical when dense solids are compared with similar structure types.²⁵ Additional details concerning the effects of entropy and the pV term are discussed in the Supporting Information (SI), with particular reference to LuF_3 in the YF_3 and ReO_3 structure types.

From the formation energy plots (see an example of the convex hull plot in the SI), the energies above the convex hull, E^{full} , were then evaluated as $E^{\text{full}}(\text{MX}_3) = E_f(\text{MX}_3) - \min[E_f(\text{MX}_3)]$, where $\min[E_f(\text{MX}_3)]$ belongs to the MX_3 compound with the lowest formation energy among all different polymorphs. Figure S1 shows an example of how we determine the convex hull of a Bi_mX_n system and related E^{full} at specific compositions, e.g., BiX_3 .

DFT calculations were performed using the projected-augmented-wave potentials,^{26,27} as implemented in VASP,^{28,29} with the following electrons treated explicitly: Bi [$6s^26p^3$], Y [$4s^24p^64d^15s^2$], Lu [$5s^25p^66d^16s^2$], F [$2s^22p^5$], Cl [$3s^23p^5$], Br [$4p^24p^5$], and I [$5s^25p^5$]. A kinetic-energy cutoff of 520 eV and a Γ -centered Monkhorst–Pack k -point mesh³⁰ were automatically generated along each reciprocal vector \vec{b}_i with a number of k -points $N_i = \max(1, l \times |\vec{b}_i| + 0.5)$ where l is the k -point line density with $l = 25$. The exchange and correlation energy was evaluated by the generalized gradient approximation, within the Perdew–Burke–Ernzerhof (PBE) functional.³¹ Van der Waals forces were captured by Grimme’s method (i.e., DFT-D3 employing zero damping).³² The total energy was considered converged within 1×10^{-5} eV. In all cases, both the volume and internal coordinates were optimized until the forces were less than 0.01 eV Å⁻¹. Whenever possible, the symmetry of each prototype structure was preserved in these calculations (see the section on the structure description). For high-pressure calculations, $H = E + pV$ was used instead of E ,

and all structures were relaxed using the same parameters as those stated above.

The band gaps of the halides were computed from the fully optimized structures (i.e., volume, shape, and internal coordinates) using the HSE06 hybrid functional³³ with van der Waals corrections. Because of the cost of the hybrid functional calculations, the total energies and geometries were converged within the prescribed tolerances set by the pymatgen library.³⁴ Spin–orbit coupling (SOC) effects were included by performing a single-point energy calculation on the fully relaxed HSE06+D3 structures. The inclusion of SOC has been found necessary³⁵ to describe accurately the electronic structures of compounds containing heavy elements, such as Bi and Pb. The band gaps were estimated from the total densities of states (DOSS) computed on k -point grids, including the special inequivalent symmetry points of the Brillouin zone of each polymorph. The electron localization function (ELF)³⁶ was computed with the PBE functional (on the fully relaxed PBE+D3 geometries) to establish the role of lone pairs in specific structures.

RESULTS AND DISCUSSION

Selection of Prototype Structures. We have considered the six structure types shown in Table 1 and Figure 1, for a

Table 1. Space Group, Coordination Number (CN) of the Metal Site, and Structural Dimensionality of the Different Structure Types Considered in This Study

type	space group	CN	dimensionality	comment	ref
BiI_3	$R\bar{3}m$	6	2D-layered	ABCABC stacking	37
YCl_3	$C2/m$	6	2D-layered	ABAB stacking	38
PuBr_3	$Ccmm$	8	2D-layered	ABAB stacking	39
ReO_3	$Pm\bar{3}m$	6	3D	perovskite-type framework	40
YF_3	$Pnma$	9	3D	3D complex structure	41
LaF_3	$P\bar{3}c1$	9	3D	tetragonite	42

total of 72 trihalides, known and hypothetical, spanning all combinations of the three metals (Bi, Lu, and Y) and four halogens (i.e., F, Cl, Br, and I). In addition, we have examined three other structure types, ZrI_3 , UCl_3 , and BiF_3 (gananite), whose results are shown in Figure S2 and Table S1. The initial

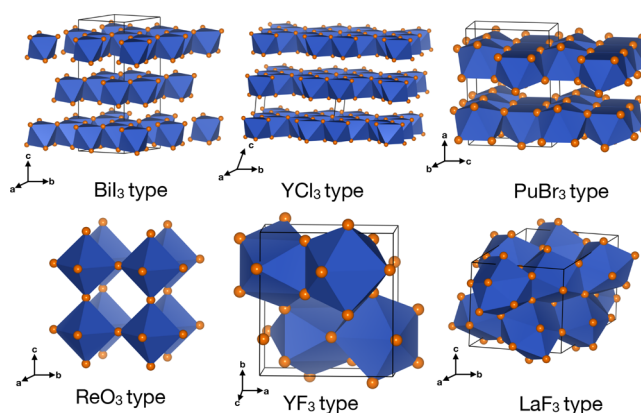


Figure 1. Six structure types explored for each system: the BiI_3 , YCl_3 , PuBr_3 , ReO_3 , YF_3 , and LaF_3 structures. The polyhedra show the metal coordination in each structure type.

structures for energy minimization and geometry optimization were taken from the Inorganic Crystal Structure Database unless stated otherwise.

Table 1 provides the geometrical characteristics of each structure type, including the coordination number (CN) of the metal and the structural dimensionality (2D- or 3D-layered network). Of the three metals studied, Bi was chosen as a potential replacement of toxic Pb in conventional hybrid perovskite solar cells, as discussed earlier. Yttrium (Y; 0.90 Å) and lutetium (Lu; 0.86 Å) are smaller in ionic radii than Bi (1.03 Å) when occupying 6-coordinated sites and are thus potential candidates to form a ReO_3 structure type. In addition, the electronic configurations of Y^{3+} and Lu^{3+} are closed-shell, unlike most of the rare-earth elements, and therefore avoid spin-polarized calculations.

BiI_3 and YCl_3 compounds form very similar layered structures, with the major difference in the different stacking arrangements of the layers (see **Figure 1** and **Table 1**). The PuBr_3 structure type is also layered and has the same stacking arrangement as YCl_3 (ABAB) but with a higher CN of the metal site (8) than YCl_3 (6). The PuBr_3 structure type was included because a number of rare-earth compounds are known to form with this structure type.²⁴

Table 2 compares the performance of our computational methodology in describing the lattice constants of the known

Table 2. Differences (%) in the Lattice Parameters and Unit Cell Volume between DFT (PBE+D3)-Calculated Values and Experiments

structure	<i>a</i>	<i>b</i>	<i>c</i>	ref
BiF_3	-0.26	1.10	1.12	41
BiCl_3	1.08	-3.67	1.66	43
BiBr_3	-0.72	-0.47	0.67	44
BiI_3	1.22	1.22	1.26	37
YF_3	0.18	1.19	2.18	41
YCl_3	-0.15	-0.44	-0.30	38
YI_3	0.30	0.30	0.72	45

MX_3 structures for Bi and Y. More details are given in the SI. Almost all of our lattice constants from DFT agree within 2% of the experimental values. Because a number of layered structures are considered (e.g., BiI_3 and YCl_3 types), van der Waals forces are treated explicitly to describe correctly the energetics and thus the structural features.³² As shown in **Table 3**, the van der Waals corrections significantly improve the predictions of the lattice parameters and volumes of layered structures such as BiI_3 . As expected, the largest improvement is observed for the *c* lattice parameters, which reflects the layer

Table 3. Comparison with Experiments of DFT-Calculated Lattice Parameters (Å) and Unit Cell Volumes for BiI_3 (Å³) for Calculations with and without van der Waals Corrections^a

	<i>a</i>	<i>c</i>	<i>a/c</i>	<i>V</i>
PBE	7.843 (4.35)	23.163 (11.79)	2.953 (7.13)	1233.91
PBE+D3	7.608 (1.22)	20.981 (1.26)	2.758 (0.04)	1051.67
Exp ³⁷	7.516	20.720	2.757	1013.66

^aThe ratio between *a* and the lattice constant along the stacking direction is also provided [in parentheses: the relative variation (%) to the experiment].

separation, and the *a/c* ratio reflects the quality of our simulations against experiments.

Thermodynamic Stability of MX_3 Materials. **Figure 2a** shows the computed volumes (color bar) per formula unit of MX_3 for each compound considered (*y* axis) across the six structure types identified (*x* axis). The volumes increase systematically from fluoride- to iodide-based structures, as well as from Lu^{3+} to Bi^{3+} , because of the increasing ionic radii of these ions. However, there are two exceptions to these trends: for YF_3 in the BiI_3 structure and YI_3 in the PuBr_3 type, the volumes are anomalously low. This appears to be caused by the significant distortions that occurred during structure relaxation; for example, YF_3 (in the BiI_3 type) changed dimensionality from an initial 2D to a 3D complex structure, and vice versa for YI_3 (in PuBr_3).

The thermodynamic stability for each compound is characterized by its formation energy and energy above the convex hull (E^{hull}) for different structure types. The color bar of **Figure 2b** shows the energy above the convex hull (in kJ mol⁻¹ per MX_3) for each structure type (*x* axis) and compound (*y* axis). White areas indicate polymorphs that are not expected to form under any conditions, whereas blue areas show stable structures (dark blue) or potential metastable structures (in lighter shades of blue). Structures identified experimentally are boxed with white halos. We chose an upper bound of E^{hull} of 20.0 kJ mol⁻¹ per MX_3 (~207 meV per MX_3 and ~52.0 meV per atom, respectively) as the threshold between the metastable and unstable structures. Sun et al.⁴⁶ have recently proposed a threshold for E^{hull} of ~70 meV atom⁻¹ between the metastable and unstable structures, and our upper bound broadly follows this prescription.

As shown in **Figure 2b**, the DFT calculations reproduce the correct experimental polymorphs in virtually all cases (see the white boxes), with E^{hull} close to or equal to 0.00 kJ mol⁻¹. Given the structural similarity of the BiI_3 and YCl_3 structure types, the values of E^{hull} for each compound with these two structure types are very similar. The only discrepancy between our DFT predictions and the experimental data is found for BiCl_3 , where DFT suggests a 2D BiI_3 (or YCl_3) structure type, whereas a 3D YF_3 structure type was reported experimentally.⁴³ However, the energy of the reported structure is only 6.4 kJ mol⁻¹ above the convex hull, and the DFT calculation for this structure nicely reproduces the molecular nature of the bonding,⁴³ with three short Bi–Cl bonds and several much longer ones.

In general, as shown in **Figures 2a,b**, the stability of ReO_3 structure types decreases upon expansion of the volume of either the M cation or X halide or both. We find that LuF_3 has the lowest energy above the hull ($E^{\text{hull}} \sim 7.8$ kJ mol⁻¹ per formula unit); hence, LuF_3 is the best candidate for adopting the ReO_3 structure type.

In addition to LuF_3 in the ReO_3 prototype, we have identified other stable or metastable structures, including YCl_3 , BiCl_3 , BiF_3 , YBr_3 , YF_3 , BiBr_3 , and LuF_3 in the PuBr_3 structure type and BiF_3 and YF_3 in the LaF_3 structure type. The PuBr_3 structure both has a high CN (8) on the metal site and is 2D-layered, which is placed between $\text{YCl}_3/\text{BiI}_3$ (low CN and dimensionality) and LaF_3/YF_3 (high CN and dimensionality). Therefore, most of these predicted compounds in the PuBr_3 structure type are close to the convex hull.

In **Figure 2b**, other general trends can be identified and serve to rationalize the relative stabilities of the these MX_3 polymorphs. For example, we observe that Lu-based

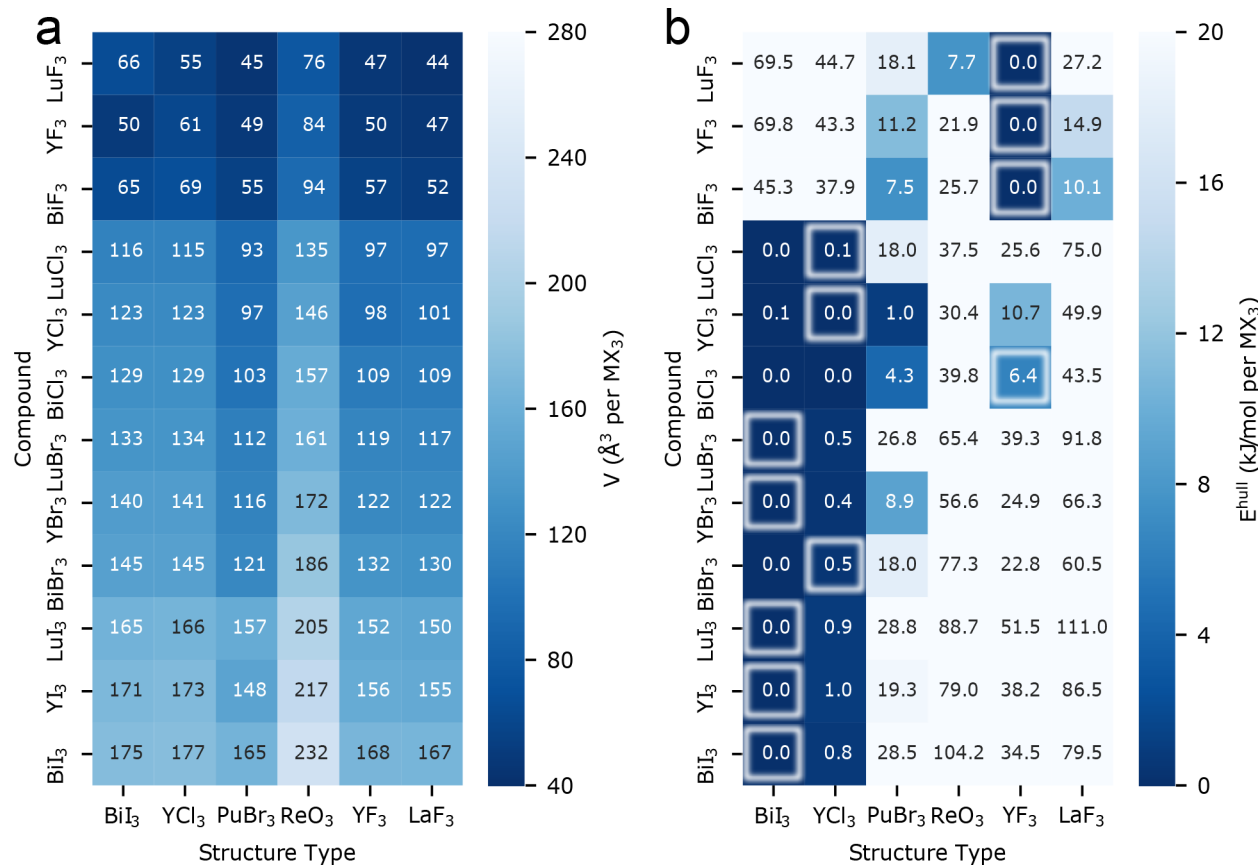


Figure 2. (a) DFT-computed unit cell volumes (V in \AA^3 per MX_3) per unit formula of MX_3 . (b) DFT-calculated formation energy above the convex hull (E_{hull} in kJ mol^{-1} per MX_3). The experimentally identified phases are boxed with white halos.

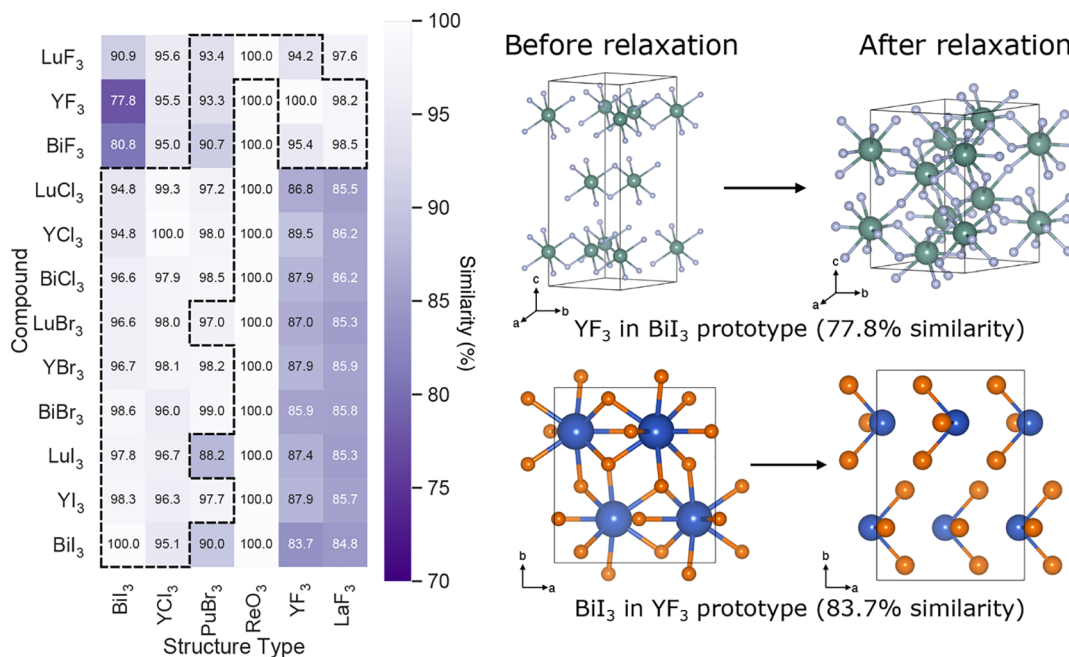


Figure 3. Structural similarity (%) between relaxed compounds and their prototypes based on the minimized d_{RMS} computed for each compound and a reference prototype. The dashed black lines are guides for the eye and map the stable or metastable structures identified in Figure 2b. Two examples, YF_3 in the BiI_3 structure type and BiI_3 in the YF_3 structure type, are shown here.

compounds in the BiI_3 structure type strongly prefer the larger anions, Cl^- , Br^- , and I^- , as demonstrated by their low energies above the hull.

It is also important to verify the relative distortions of compounds investigated in this study in comparison to their prototypical structures, e.g., ReO_3 , BiI_3 , and LaF_3 . To this end,

we utilize a structure matching algorithm,⁴⁷ which computes the minimized root-mean-square distances. This is defined as $d_{\text{RMS}} = \sqrt{n/V_{\text{avg}}} \sqrt{(\sum_{i=1}^n d_i^2)/n}$ between each compound and a reference structure, where d_i is the Cartesian distances between the i th site between two structures, n is the total number of sites, and V_{avg} is the volume of the average lattice of the two structures compared. Our reference structures are the prototypical experimental structures; for example, if we consider LuF_3 in the ReO_3 structure type, its reference structure would be set by the atomic arrangement in ReO_3 ($Pm\bar{3}m$). Thus, a value of $d_{\text{RMS}} = 0$ means that the compound has the structure of its prototype and, hence, without any distortion. In contrast, large values of d_{RMS} suggest large distortions after relaxation.

Figure 3 shows the relative changes in percent (of d_{RMS}), here termed similarity, between different compounds and their structure prototypes of origin, where dark purple represents large distortion from the prototype structure of reference. Note that 100% similarity matches with $d_{\text{RMS}} = 0$ and 0% stands for $d_{\text{RMS}} = 1$. All compounds with the ReO_3 structure type have 100% similarity due to the symmetry constraint imposed during the relaxation process.

By relating trends of similarity (or d_{RMS}) and thermodynamic stability (**Figure 2b**), a number of observations can be made. (i) At first glance, one can draw a unidirectional link between structures with high thermodynamic stability (i.e., $E^{\text{hull}} \sim 0$ kJ per formula unit) and structures with high similarity near 100% (or close to $d_{\text{RMS}} = 0$). For example, most chloride, bromide, and iodide compounds in the $\text{BiI}_3/\text{YCl}_3$ types are thermodynamically stable (**Figure 2b**) and, hence, show appreciable similarity with their prototypes, i.e., small distortions after relaxation. Exceptions to this trend are YCl_3 and BiCl_3 in the YF_3 structure type. In particular, YCl_3 forms a layered-type structure, whereas BiCl_3 forms an almost isolated molecular structure, most likely because of the lone pair of Bi^{3+} (as discussed in the next section). (ii) Interestingly, one observes that when fluorine compounds, such as LaF_3 and YF_3 , are anion-exchanged with the larger halides Cl^- , Br^- , or I^- , low values of similarity (i.e., large d_{RMS} values) and low thermodynamic stabilities (**Figure 2b**) are found. From a closer inspection of the structures of these compounds, we observed their transformation from 3D compact structures to layered-type structures. Similarly, a transformation implying a change of the dimensionality from 2D to 3D can be observed when iodine is exchanged with fluorine, as in the compounds in the top-left side of **Figure 3**. (iii) Another observation is that high values of similarity, equivalent to low values of d_{RMS} , cannot guarantee low or zero E^{hull} . While most compounds in the ReO_3 structure type are thermodynamically unstable (except for LuF_3), they appear less distorted after relaxation, which we link to the constraint of symmetry and the size of the unit cell adopted.

Role of the Lone Pair in BiX_3 Structures. We move now to analysis of the electronic structure of the known experimental structure types (see **Table 1**), beginning with consideration of the lone-pair effects in the bismuth(III) compounds. It is well established that a wide range of lead(II) and bismuth(III) compounds exhibit stereochemically active s^2 lone pairs in systems ranging from inorganic⁴⁸ and hybrid perovskites⁴⁹ to metal–organic frameworks,^{50,51} so it is expected that these effects might be seen in the bismuth halides. We explore this behavior in the BiX_3 phases by

analyzing the ELF, which enables us to localize the electron lone pairs around bismuth(III) (**Figure 4**). For comparison, we also show the ELF functions for the corresponding yttrium(III) phases, where no lone-pair effect is expected.

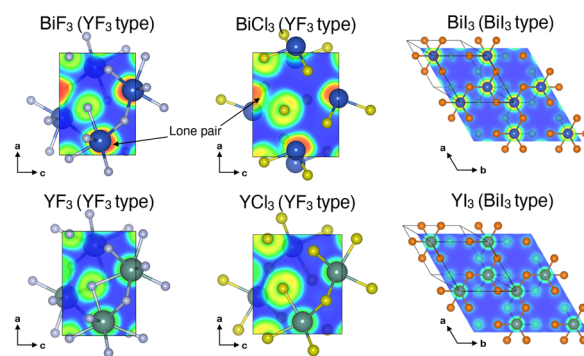


Figure 4. Computed ELFs for BiF_3 , BiCl_3 , BiI_3 , YF_3 , YCl_3 , and YI_3 in the structure type shown in parentheses. Note that BiBr_3 and YBr_3 are very similar to the iodide analogues. Color mapping of the ELF value is shown from 0 (blue) to 1 (red).

In ELF calculations, values near 0.5 are indicative of the delocalization of charge similar to a homogeneous electron gas, whereas $\text{ELF} = 1$ suggests areas matching high electron localization. From **Figure 4**, both BiF_3 and BiCl_3 show large ELF values (~ 0.8) near the Bi^{3+} cations and the shape of the domain appears highly anisotropic, suggesting significant localization of the lone pair. The presence of lone-pair effects can directly affect the symmetry and unit cell dimensions of the crystal structures.⁴⁸ For example, in BiF_3 , the lone pair causes an elongation of the c axis, increasing the c/a ratio to 0.75;⁴¹ this can be compared with a value of 0.71 in YF_3 , where the lone pair is not present. In BiCl_3 , which is virtually molecular, one can observe the arrangement of pyramidal BiCl_3 moieties that are held together by van der Waals forces, much as one would find in the structure of ammonia. Because of the distortion imparted by the highly localized lone pair, the overall dimensionality and CN of Bi^{3+} are reduced. This may lead to the confinement of electrons, which is partly responsible for the large band gaps in BiCl_3 and BiF_3 (see **Figure 5**). However, in the case of BiBr_3 and BiI_3 (**Figure 4**), the lone pairs are not active and the ELFs are very similar to those of the Y structures. The tendency of lone-pair effects to be stronger with more electronegative ions has been seen in other systems, such as the PbO -layered structure (driven by the lone pair on Pb) compared with the cubic rock-salt structure in PbS , PbSe , and PbTe .⁵² To some extent, however, the lone-pair effect can be influenced by the structure itself because we note that BiI_3 in a hypothetical YF_3 structure type forms a pyramidal molecular species like that seen experimentally in BiCl_3 (**Figure S5**).

Band-Gap Characteristics of MX_3 . We now move our attention to the optoelectronic properties of the MX_3 -based materials. **Figure 5a** shows the band-gap values (E_g) computed with the HSE06 hybrid functional, while **Table 4** compares our predictions with the existing experimental measurements of E_g . When the predicted values of the band gap are benchmarked against the experimentally reported values in **Table 4**, we observe that our data with the HSE06 hybrid functional are more accurate. As in hybrid perovskite materials, the quantitative description of E_g requires a higher level of theory

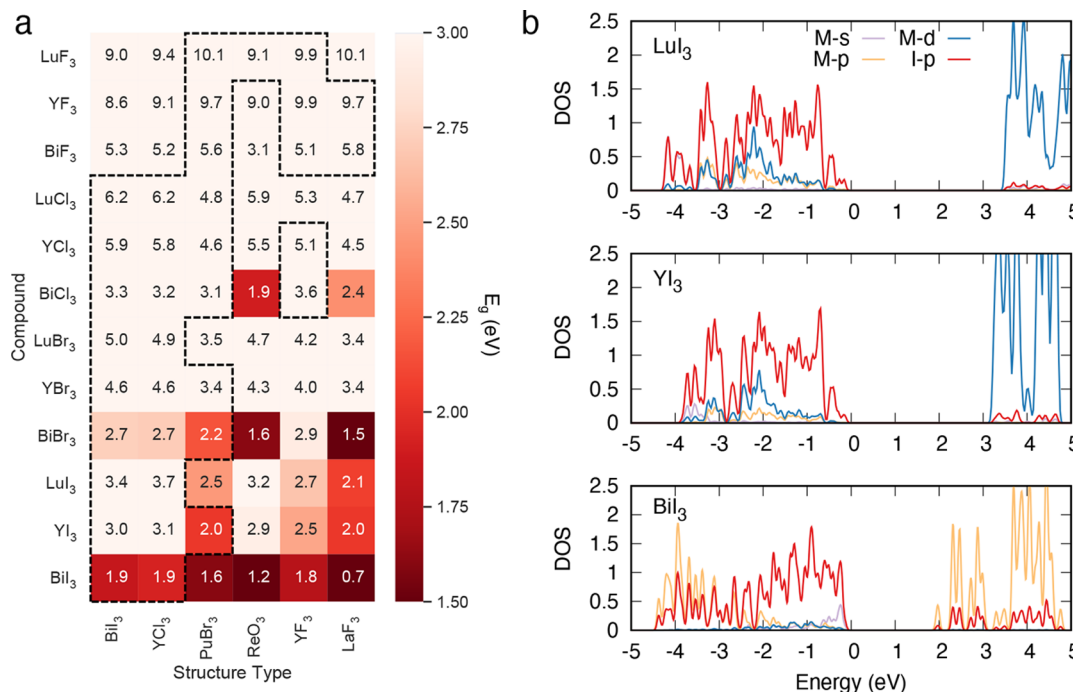


Figure 5. (a) Computed energy band gaps (E_g in eV) at the HSE06+D3+SOC level of theory. The dashed black lines are guides for mapping the stable or metastable structures identified in Figure 2b. (b) pDOS on selected atomic orbitals of MI_3 ($\text{M} = \text{Lu}, \text{Y}$, and Bi) in the BiI_3 structure type.

Table 4. Comparison of E_g (eV) between the Experiment and DFT-Calculated Values (Same Structure Type)

compound	$E_{g,\text{DFT}}$	$E_{g,\text{Exp}}$
YF_3	9.9	10.30 ⁵⁴
BiCl_3	3.6	3.37 ⁵⁵
BiBr_3	2.7	2.66 ⁵⁵
BiI_3	1.9	1.67, ⁵⁶ 1.8 ^{19,21}

(e.g., hybrid functionals or many-body treatments, such as GW), together with SOC corrections.⁵³

The E_g values in halides decrease upon moving down the halogen group, i.e., from F^- to I^- , as expected. For example, in Bi-containing compounds (experimental structure type), the band gap decreases systematically as BiF_3 (5.1 eV) > BiCl_3 (3.6 eV) > BiBr_3 (2.7 eV) > BiI_3 (1.9 eV). As for the metal site, Bi-based compounds always show the lowest band gaps compared to Y- and Lu-based compounds, with Y materials showing slightly lower band gaps than Lu compounds.

We complement this analysis with the projected density of states (pDOS) on specific atomic orbitals of selected structures to identify the orbital character of both valence and conduction bands. As an example, the PDOS of LuI_3 , YI_3 , and BiI_3 in the BiI_3 structure type are shown in Figure 5b. For valence bands, LuI_3 and YI_3 are dominated by the I 5p states, whereas in BiI_3 , Bi 6s also contributes significantly to the DOS. The conduction bands of LuI_3 and YI_3 are mostly dominated by Y 3d and Lu 4d with small contributions from the I 5p levels, whereas the BiI_3 conduction band is dominated mostly by the Bi 6p and I 5p states. Therefore, the Bi 6s and Bi 6p states in the band edges result in a much smaller band gap for BiI_3 compared with those for YI_3 and LuI_3 . As aforementioned for the halide species, the larger the ionic radius of the metal, the lower the band gap.⁵⁷

It is often observed that band gaps in materials decrease under external pressure; for example, in hybrid halide

perovskites, high-pressure compression can induce a redshift of the PL energy.⁵⁸ Having explored a number of BiX_3 phases in different structures (e.g., BiI_3 in the PuBr_3 structure), we can now explain some of the observations that have been made in various high-pressure studies of BiI_3 . Experimentally, Darnell et al.⁵⁹ suggested that there is a phase transition of BiI_3 at ~ 2.5 GPa, while Hsueh et al.⁶⁰ showed a phase transition from a rhombohedral ($R\bar{3}$) structure to a monoclinic ($P2_1/c$) distorted PuBr_3 -type structure beyond ~ 7 GPa. In addition, Devidas et al.⁶¹ reported that BiI_3 becomes metallic at ~ 1.5 GPa and observed another phase transition to a monoclinic ($P2_1/c$) structure at ~ 8.8 GPa. To elucidate the relative stabilities of different forms of BiI_3 at different pressures, we present in Figure 6 the computed formation enthalpies above the convex hull H^{bulk} from ambient pressure up to 9 GPa. Figure 6 shows that, below 3 GPa, the 6-coordinated layered BiI_3 -type structure is the most stable for BiI_3 , as observed experimentally. At a pressure of ~ 3 –4 GPa, we predict a phase transition from the BiI_3 structure type to monoclinic distorted phase from the higher coordinated PuBr_3 structure type, and it remains stable for pressures of up to 9 GPa, which is also in agreement with experiments.^{60,62} Note that the 3D YF_3 and LaF_3 structure types are not expected to be stable at any pressure. We have also performed DFT calculations on the experimentally distorted PuBr_3 structure type that Hsueh et al.⁶⁰ reported at different pressures, and the results are similar to our PuBr_3 -type results (Figure S6) in the high-pressure (>2 GPa) region, although it transformed back to the layered 6-coordinated YCl_3 structure type in the low-pressure (0–2 GPa) region. Our lattice constants for the PuBr_3 form of BiI_3 at 8 GPa are in agreement with synchrotron X-ray data collected at ~ 7.31 GPa by Hsueh et al.⁶⁰ (Table S2). The band gap of this high-pressure phase at 8 GPa was calculated (HSE06+D3+SOC) and found to be significantly lower (~ 1.0 eV) than that of the layered BiI_3 structure type (~ 1.6 eV) at ambient pressure.

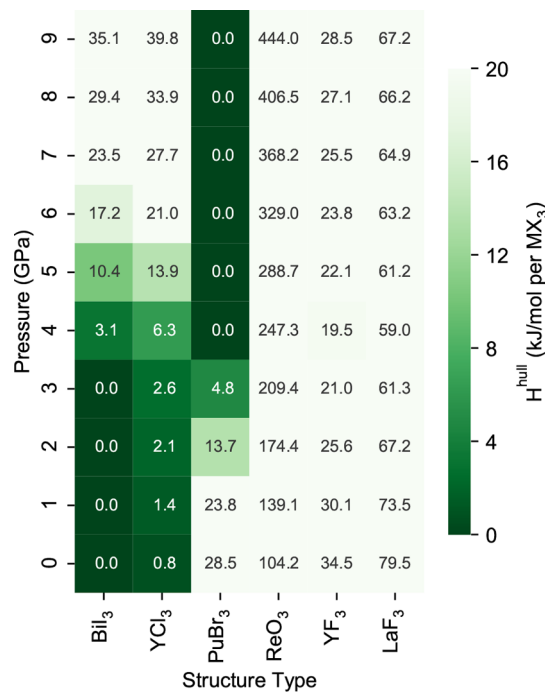


Figure 6. DFT-calculated formation enthalpy above the convex hull (H_{hull} in kJ mol^{-1} per MX_3) of the BiI_3 composition in different structure types under pressure.

Experimental Attempts to Make the ReO_3 Form of LuF_3 . On the basis of our DFT calculations (Figure 2b), LuF_3 has the lowest E_{hull} with the ReO_3 structure type, so it is expected to be the best candidate for adopting that structure. Zalkin and Templeton⁶² reported a mixture of unresolved phases in their solution preparation of LuF_3 , which further encouraged us to explore this idea. They also observed that heating their initial reaction product led to formation of the orthorhombic YF_3 structure type. Experimental attempts to synthesize LuF_3 have therefore been carried out. Following their recipe, 15 mg of Lu_2O_3 was fully dissolved in 5 mL of concentrated hydrochloric acid at 50 °C, and the solution was then neutralized by a NH_4OH solution. A few drops of concentrated hydrofluoric acid (47 wt % H_2O) was added to the solution to obtain a white precipitate. The mixture was

centrifuged, washed with deionized water, and then dried in air. Zalkin and Templeton were unable to solve the complicated pattern, but we have found that it is a complex acid hydrate, $(\text{H}_3\text{O})\text{Lu}_3\text{F}_{10}\cdot\text{H}_2\text{O}$, and is isomorphous with $(\text{H}_3\text{O})\text{Yb}_3\text{F}_{10}\cdot\text{H}_2\text{O}$ ⁶³ (Figure 7, right). $(\text{H}_3\text{O})\text{Lu}_3\text{F}_{10}\cdot\text{H}_2\text{O}$ has cubic symmetry and space group $Fd\bar{3}m$ with $a = 15.2967(5)$ Å. Structure solution was carried out using TOPAS Academic 6.0, and Pawley refinement is shown in Figure 7, top left (details on the structure determination and associated crystallographic information are reported in the SI). After heating of the powder at 100 °C for 1 h, an orthorhombic phase with the YF_3 structure type was obtained, as described by Zalkin and Templeton⁶² (powder X-ray diffraction results are shown in Figure 7, left bottom). Other synthetic methods, e.g., thermal evaporation until dryness at 90 °C or hydrothermal synthesis using $\text{Lu}(\text{NO}_3)_3$ or Lu_2O_3 and diluted hydrofluoric acid at 120 °C, also give the orthorhombic YF_3 structure type. We have found no evidence for the formation of ReO_3 modification of LuF_3 .

CONCLUSIONS

In this study, systematic first-principles calculations have been used to map the chemical space of BiX_3 halides and the analogous MX_3 compositions with $M = \text{Y}$ and Lu . Calculations for 12 different MX_3 compositions, each with 9 potential polymorphs, reveal the thermodynamic stabilities of MX_3 in different structure types. The results for the thermodynamically stable phases are in very good agreement with experiments. The qualitative trends follow the radius ratios of the cation M and anion X (r_M/r_X) such that the CN of the cations increases as the anion size decreases. For example, the smallest anion, F^- , strongly favors the highly coordinated environment that is found in the YF_3 structure, whereas larger anions, especially I^- , prefer a 6-coordinated cation environment and form YCl_3 or BiI_3 structures.

It is also found that the dimensionality of the crystal structures of MX_3 is strongly correlated to the size of the anion. For compositions with large anions, such as Br^- and I^- , a lower-dimensional structure is favored, e.g., BiI_3 (2D), YCl_3 (2D), PuBr_3 (2D), ZrI_3 (1D), and AlI_3 (0D, molecular dimer). The reason for this is that the cation–anion packing density plays an important role in determining its dimensionality, and a higher cation–anion packing density is favored energetically.

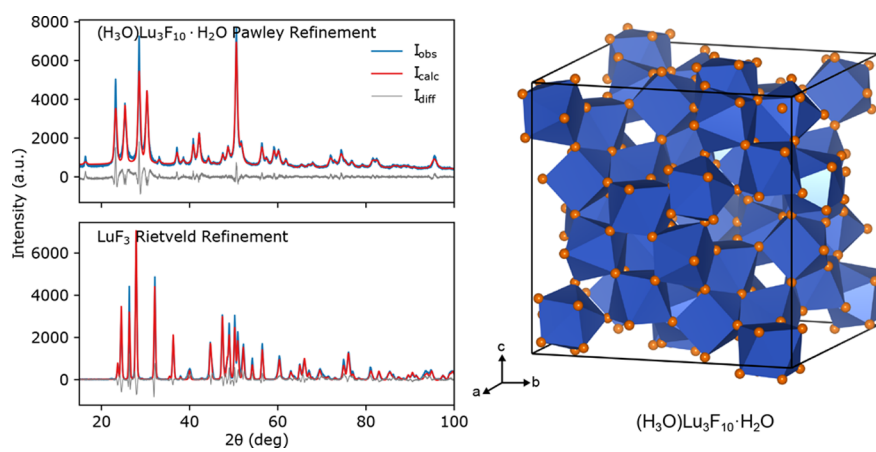


Figure 7. Left: Pawley refinement (top) for the white precipitates of $(\text{H}_3\text{O})\text{Lu}_3\text{F}_{10}\cdot\text{H}_2\text{O}$ with space group $Fd\bar{3}m$ and $a = 15.2967(5)$ Å and Rietveld refinement (bottom) of LuF_3 in $Pnma$ with $a = 6.1149(3)$ Å, $b = 6.7595(3)$ Å, and $c = 4.5064(3)$ Å. Right: Crystal structure of $(\text{H}_3\text{O})\text{Lu}_3\text{F}_{10}\cdot\text{H}_2\text{O}$ (H_2O molecules are not shown).

From Figure 2a, it is shown that, with the same CN of 6, the unit cell volumes of the high-dimensional ReO_3 structure types are much higher than those of the corresponding layered $\text{BiI}_3/\text{YCl}_3$ structure types in the case of large anion (Br^- and I^-). van der Waals interactions also provide additional stabilization in denser structures and not only to the layered ones. We note that, even without considering van der Waals forces explicitly in our calculations, the layered $\text{BiI}_3/\text{YCl}_3$ structure types remain the most stable structures for large anions (Figure S4). This observation shows that layered structures are not solely stabilized by van der Waals forces. However, when van der Waals forces are not included in the calculations, the ReO_3 structure type is predicted to be favored relative to the YF_3 structure type for LuF_3 (Figure S4). In this case, the observed structure is clearly stabilized by the van der Waals forces.

Taken together, these considerations confirm that, in order to form a 3D 6-coordinated ReO_3 -type structure, small anions, e.g., F^- , together with small cations such as Al^{3+} , Sc^{3+} , or smaller transitional metal cations, are required. LuF_3 follows this trend, although our experimental synthesis also showed that even LuF_3 cannot form an ReO_3 -type framework. We find that other candidates with desirable properties for PV applications, such as BiI_3 in the ReO_3 structure type, are not energetically accessible because of their low packing densities. Even under pressure, it is not possible to stabilize BiI_3 with the ReO_3 structure type because the denser PuBr_3 structure type becomes more stable.

The important role of electron localization as lone pairs in the BiX_3 compounds has been seen in the cases of both BiF_3 and BiCl_3 , in terms of both their structures and band gaps. Although it is widely believed that stereochemically active lone pairs are particularly prevalent in systems containing more electronegative anions, e.g., fluoride, chloride, and oxide, we also find that even BiI_3 would be distorted if it was to adopt a YF_3 structure type. It would appear that the ability of different structure types to accommodate distortions is more important than was hitherto believed in determining the sensitivity to lone-pair effects.

■ ASSOCIATED CONTENT

SI Supporting Information

The Supporting Information is available free of charge at <https://pubs.acs.org/doi/10.1021/acs.inorgchem.9b03214>.

Convex hulls of BiX (with $X = \text{F}, \text{Cl}, \text{Br}$, and I ; Figure S1), details of other structure types also considered in this study (Figure S2 and Table S1), effects of pressure on a number of structure types (Table S2), computed formation energies and volumes using the PBE and PBE +D3 functionals, respectively (Figures S3 and S4), ELF plots of selected structures (Figure S5), formation enthalpies of the BiI_3 composition in different structure types (Figure S6), details on the effects of entropy and pV terms on the thermodynamic stability of different structure types (Table S3), and a final section on the experimental method and determination of the newly synthesized $(\text{H}_3\text{O})\text{Lu}_3\text{F}_{10}\cdot\text{H}_2\text{O}$ structure, including Tables S4–S6 (PDF)

■ AUTHOR INFORMATION

Corresponding Author

Pieremanuele Canepa – Department of Materials Science and Engineering, National University of Singapore, Singapore

119077 Singapore; orcid.org/0000-0002-5168-9253;
Email: pcanepa@nus.edu.sg

Authors

Zeyu Deng – Department of Materials Science and Engineering, National University of Singapore, Singapore 119077 Singapore; orcid.org/0000-0003-0109-9367

Fengxia Wei – Institute of Materials Research and Engineering, A*STAR, Singapore 138632 Singapore

Yue Wu – Department of Materials Science and Engineering, National University of Singapore, Singapore 119077 Singapore; orcid.org/0000-0003-2874-8267

Ram Seshadri – Materials Department and Materials Research Laboratory, University of California, Santa Barbara, California 93106, United States; orcid.org/0000-0001-5858-4027

Anthony K. Cheetham – Department of Materials Science and Engineering, National University of Singapore, Singapore 119077 Singapore; Materials Department and Materials Research Laboratory, University of California, Santa Barbara, California 93106, United States; orcid.org/0000-0003-1518-4845

Complete contact information is available at:
<https://pubs.acs.org/10.1021/acs.inorgchem.9b03214>

Notes

The authors declare no competing financial interest.
All the simulation outputs and inputs are available at [10.5281/zenodo.3627648](https://zenodo.3627648).

■ ACKNOWLEDGMENTS

P.C., Z.D., and A.K.C. acknowledge financial support by the Singapore Ministry of Education Academic Fund Tier 1 (Grants R-284-000-186-133 and R-284-000-194-114), as well as the NUS-funded Green Energy Programme (Grant R-284-000-185-731). The computational work for this Article was performed on resources of the National Supercomputing Centre, Singapore (<https://www.nscc.sg>).

■ REFERENCES

- (1) Blasse, G. Scintillator materials. *Chem. Mater.* **1994**, *6*, 1465–1475.
- (2) Cui, X.; Hu, T.; Wang, J.; Zhang, J.; Zhong, X.; Chen, Y.; Li, X.; Yang, J.; Gao, C. Ionic Transportation and Dielectric Properties of $\text{YF}_3\text{:Eu}^{3+}$ Nanocrystals. *Nanomaterials* **2018**, *8*, 995.
- (3) Trnovcová, V.; Garashina, L.; Škulba, A.; Fedorov, P.; Číčka, R.; Krivandina, E.; Sobolev, B. Structural aspects of fast ionic conductivity of rare earth fluorides. *Solid State Ionics* **2003**, *157*, 195–201.
- (4) Wang, F.; Liu, X. Recent advances in the chemistry of lanthanide-doped upconversion nanocrystals. *Chem. Soc. Rev.* **2009**, *38*, 976.
- (5) Yan, R. X.; Li, Y. D. Down/Up Conversion in Ln^{3+} -Doped YF_3 Nanocrystals. *Adv. Funct. Mater.* **2005**, *15*, 763–770.
- (6) Kojima, A.; Teshima, K.; Shirai, Y.; Miyasaka, T. Organometal Halide Perovskites as Visible-Light Sensitizers for Photovoltaic Cells. *J. Am. Chem. Soc.* **2009**, *131*, 6050–6051.
- (7) Lee, M. M.; Teuscher, J.; Miyasaka, T.; Murakami, T. N.; Snaith, H. J. Efficient Hybrid Solar Cells Based on Meso-Superstructured Organometal Halide Perovskites. *Science* **2012**, *338*, 643–647.
- (8) Snaith, H. J. Perovskites: The Emergence of a New Era for Low-Cost, High-Efficiency Solar Cells. *J. Phys. Chem. Lett.* **2013**, *4*, 3623–3630.
- (9) Protesescu, L.; Yakunin, S.; Bodnarchuk, M. I.; Krieg, F.; Caputo, R.; Hendon, C. H.; Yang, R. X.; Walsh, A.; Kovalenko, M. V. Nanocrystals of Cesium Lead Halide Perovskites (CsPbX_3 , $X = \text{Cl}, \text{Br}$,

- and I): Novel Optoelectronic Materials Showing Bright Emission with Wide Color Gamut. *Nano Lett.* **2015**, *15*, 3692–3696.
- (10) Kasel, T. W.; Deng, Z.; Mroz, A. M.; Hendon, C. H.; Butler, K. T.; Canepa, P. Metal-free perovskites for non linear optical materials. *Chem. Sci.* **2019**, *10*, 8187–8194.
- (11) Morss, L. R.; Siegal, M.; Stenger, L.; Edelstein, N. Preparation of cubic chloro complex compounds of trivalent metals: $\text{Cs}_2\text{NaMCl}_6$. *Inorg. Chem.* **1970**, *9*, 1771–1775.
- (12) Slavney, A. H.; Hu, T.; Lindenberg, A. M.; Karunadasa, H. I. A Bismuth-Halide Double Perovskite with Long Carrier Recombination Lifetime for Photovoltaic Applications. *J. Am. Chem. Soc.* **2016**, *138*, 2138–2141.
- (13) McClure, E. T.; Ball, M. R.; Windl, W.; Woodward, P. M. $\text{Cs}_2\text{AgBiX}_6$ ($X = \text{Br}, \text{Cl}$): New Visible Light Absorbing, Lead-Free Halide Perovskite Semiconductors. *Chem. Mater.* **2016**, *28*, 1348–1354.
- (14) Volonakis, G.; Filip, M. R.; Haghhighirad, A. A.; Sakai, N.; Wenger, B.; Snaith, H. J.; Giustino, F. Lead-Free Halide Double Perovskites via Heterovalent Substitution of Noble Metals. *J. Phys. Chem. Lett.* **2016**, *7*, 1254–1259.
- (15) Wei, F.; Deng, Z.; Sun, S.; Xie, F.; Kieslich, G.; Evans, D. M.; Carpenter, M. A.; Bristowe, P. D.; Cheetham, A. K. The synthesis, structure and electronic properties of a lead-free hybrid inorganic–organic double perovskite $(\text{MA})_2\text{KBiCl}_6$ ($\text{MA} = \text{methylammonium}$). *Mater. Horiz.* **2016**, *3*, 328–332.
- (16) Deng, Z.; Wei, F.; Sun, S.; Kieslich, G.; Cheetham, A. K.; Bristowe, P. D. Exploring the properties of lead-free hybrid double perovskites using a combined computational-experimental approach. *J. Mater. Chem. A* **2016**, *4*, 12025–12029.
- (17) Wei, F.; Deng, Z.; Sun, S.; Hartono, N. T. P.; Seng, H. L.; Buonassisi, T.; Bristowe, P. D.; Cheetham, A. K. Enhanced visible light absorption for lead-free double perovskite $\text{Cs}_2\text{AgSbBr}_6$. *Chem. Commun.* **2019**, *55*, 3721–3724.
- (18) Deng, Z.; Wei, F.; Brivio, F.; Wu, Y.; Sun, S.; Bristowe, P. D.; Cheetham, A. K. Synthesis and Characterization of the Rare-Earth Hybrid Double Perovskites: $(\text{CH}_3\text{NH}_3)_2\text{KGdCl}_6$ and $(\text{CH}_3\text{NH}_3)_2\text{KYCl}_6$. *J. Phys. Chem. Lett.* **2017**, *8*, 5015–5020.
- (19) Lehner, A. J.; Wang, H.; Fabini, D. H.; Liman, C. D.; Hébert, C.-A.; Perry, E. E.; Wang, M.; Bazan, G. C.; Chabiny, M. L.; Seshadri, R. Electronic structure and photovoltaic application of BiI_3 . *Appl. Phys. Lett.* **2015**, *107*, 131109.
- (20) Hamdeh, U. H.; Nelson, R. D.; Ryan, B. J.; Bhattacharjee, U.; Petrich, J. W.; Panthani, M. G. Solution-Processed BiI_3 Thin Films for Photovoltaic Applications: Improved Carrier Collection via Solvent Annealing. *Chem. Mater.* **2016**, *28*, 6567–6574.
- (21) Brandt, R. E.; Kurchin, R. C.; Hoye, R. L. Z.; Poindexter, J. R.; Wilson, M. W. B.; Sulekar, S.; Lenahan, F.; Yen, P. X. T.; Stevanović, V.; Nino, J. C.; Bawendi, M. G.; Buonassisi, T. Investigation of Bismuth Triiodide (BiI_3) for Photovoltaic Applications. *J. Phys. Chem. Lett.* **2015**, *6*, 4297–4302.
- (22) Evans, H. A.; Deng, Z.; Collings, I. E.; Wu, Y.; Andrews, J. L.; Pilar, K.; Tuffnell, J. M.; Wu, G.; Wang, J.; Dutton, S. E.; Bristowe, P. D.; Seshadri, R.; Cheetham, A. K. Polymorphism in $\text{M}(\text{H}_2\text{PO}_2)_3$ ($\text{M} = \text{V}, \text{Al}, \text{Ga}$) compounds with the perovskite-related ReO_3 structure. *Chem. Commun.* **2019**, *55*, 2964–2967.
- (23) Evans, H. A.; Wu, Y.; Seshadri, R.; Cheetham, A. K. Perovskite-related ReO_3 -type structures. *Nat. Rev. Mater.* **2020**, *XX*, XXX DOI: [10.1038/s41578-019-0160-x](https://doi.org/10.1038/s41578-019-0160-x).
- (24) Wells, A. F. *Structural Inorganic Chemistry*; Oxford University Press, 2012.
- (25) van de Walle, A.; Ceder, G. The effect of lattice vibrations on substitutional alloy thermodynamics. *Rev. Mod. Phys.* **2002**, *74*, 11–45.
- (26) Kresse, G.; Joubert, D. From ultrasoft pseudopotentials to the projector augmented-wave method. *Phys. Rev. B: Condens. Matter Mater. Phys.* **1999**, *59*, 1758–1775.
- (27) Blöchl, P. E. Projector augmented-wave method. *Phys. Rev. B: Condens. Matter Mater. Phys.* **1994**, *50*, 17953–17979.
- (28) Kresse, G.; Furthmüller, J. Efficient iterative schemes for ab initio total-energy calculations using a plane-wave basis set. *Phys. Rev. B: Condens. Matter Mater. Phys.* **1996**, *54*, 11169–11186.
- (29) Kresse, G.; Furthmüller, J. Efficiency of ab-initio total energy calculations for metals and semiconductors using a plane-wave basis set. *Comput. Mater. Sci.* **1996**, *6*, 15–50.
- (30) Monkhorst, H. J.; Pack, J. D. Special points for Brillouin-zone integrations. *Phys. Rev. B* **1976**, *13*, 5188–5192.
- (31) Perdew, J. P.; Burke, K.; Ernzerhof, M. Generalized Gradient Approximation Made Simple. *Phys. Rev. Lett.* **1996**, *77*, 3865–3868.
- (32) Grimme, S.; Antony, J.; Ehrlich, S.; Krieg, H. A consistent and accurate ab initio parametrization of density functional dispersion correction (DFT-D) for the 94 elements H-Pu. *J. Chem. Phys.* **2010**, *132*, 154104.
- (33) Kruckau, A. V.; Vydróv, O. A.; Izmaylov, A. F.; Scuseria, G. E. Influence of the exchange screening parameter on the performance of screened hybrid functionals. *J. Chem. Phys.* **2006**, *125*, 224106.
- (34) Ong, S. P.; Richards, W. D.; Jain, A.; Hautier, G.; Kocher, M.; Cholia, S.; Gunter, D.; Chevrier, V. L.; Persson, K. A.; Ceder, G. Python Materials Genomics (pymatgen): A robust, open-source python library for materials analysis. *Comput. Mater. Sci.* **2013**, *68*, 314–319.
- (35) Even, J.; Pedesseau, L.; Jancu, J.-M.; Katan, C. Importance of Spin–Orbit Coupling in Hybrid Organic/Inorganic Perovskites for Photovoltaic Applications. *J. Phys. Chem. Lett.* **2013**, *4*, 2999–3005.
- (36) Silvi, B.; Savin, A. Classification of chemical bonds based on topological analysis of electron localization functions. *Nature* **1994**, *371*, 683–686.
- (37) Keller, L.; Nason, D. Review of X-ray powder diffraction data of rhombohedral bismuth tri-iodide. *Powder Diffr.* **1996**, *11*, 91–96.
- (38) Templeton, D. H.; Carter, G. F. The Crystal Structures of Yttrium Trichloride and Similar Compounds. *J. Phys. Chem.* **1954**, *58*, 940–944.
- (39) Zachariasen, W. H. Crystal chemical studies of the Sr -series of elements. I. New structure types. *Acta Crystallogr.* **1948**, *1*, 265–268.
- (40) Meisel, K. Rheniumtrioxys. III. Mitteilung. Über die Kristallstruktur des Rheniumtrioxys. *Z. Anorg. Allg. Chem.* **1932**, *207*, 121–128.
- (41) Cheetham, A. K.; Norman, N.; Hope, H.; Kjekshus, A.; Klewe, B.; Powell, D. L. The Structures of Yttrium and Bismuth Trifluorides by Neutron Diffraction. *Acta Chem. Scand.* **1974**, *28a*, 55–60.
- (42) Cheetham, A. K.; Fender, B. E. F.; Fuess, H.; Wright, A. F. A powder neutron diffraction study of lanthanum and cerium trifluorides. *Acta Crystallogr., Sect. B: Struct. Crystallogr. Cryst. Chem.* **1976**, *32*, 94–97.
- (43) Nyburg, S. C.; Ozin, G. A.; Szymbański, S. T. The crystal and molecular structure of bismuth trichloride. Corrigendum. *Acta Crystallogr., Sect. B: Struct. Crystallogr. Cryst. Chem.* **1972**, *28*, 2885–2885.
- (44) von Benda, H. Zur Polymorphie des Wismuttribromids. *Z. Kristallogr. - Cryst. Mater.* **1980**, *151* (3–4), 271–285, DOI: [10.1524/zkr.1980.151.3-4.271](https://doi.org/10.1524/zkr.1980.151.3-4.271).
- (45) Jongen, L.; Meyer, G. Yttrium triiodide, YI_3 . *Acta Crystallogr., Sect. E: Struct. Rep. Online* **2005**, *61*, i151–i152.
- (46) Sun, W.; Dacek, S. T.; Ong, S. P.; Hautier, G.; Jain, A.; Richards, W. D.; Gamst, A. C.; Persson, K. A.; Ceder, G. The thermodynamic scale of inorganic crystalline metastability. *Sci. Adv.* **2016**, *2*, No. e1600225.
- (47) Wang, Y.; Richards, W. D.; Ong, S. P.; Miara, L. J.; Kim, J. C.; Mo, Y.; Ceder, G. Design principles for solid-state lithium superionic conductors. *Nat. Mater.* **2015**, *14*, 1026–1031.
- (48) Seshadri, R.; Hill, N. A. Visualizing the Role of Bi 6s “Lone Pairs” in the Off-Center Distortion in Ferromagnetic BiMnO_3 . *Chem. Mater.* **2001**, *13*, 2892–2899.
- (49) Fabini, D. H.; Siaw, T. A.; Stoumpos, C. C.; Laurita, G.; Olds, D.; Page, K.; Hu, J. G.; Kanatzidis, M. G.; Han, S.; Seshadri, R. Universal Dynamics of Molecular Reorientation in Hybrid Lead Iodide Perovskites. *J. Am. Chem. Soc.* **2017**, *139*, 16875–16884.

- (50) Ayyappan, S.; Diaz de Delgado, G.; Cheetham, A. K.; Férey, G.; Rao, C. N. R. Synthesis and characterization of a three-dimensional open-framework lead(II) carboxyethylphosphonate, $\text{Pb}_3(\text{O}_2\text{CCH}_2\text{CH}_2\text{PO}_3)_2$. *J. Chem. Soc., Dalton Trans.* **1999**, 2905–2907.
- (51) Thirumurugan, A.; Cheetham, A. K. Anionic Metal-Organic Frameworks of Bismuth Benzenedicarboxylates: Synthesis, Structure and Ligand-Sensitized Photoluminescence. *Eur. J. Inorg. Chem.* **2010**, 3823–3828.
- (52) Walsh, A.; Payne, D. J.; Egddell, R. G.; Watson, G. W. Stereochemistry of post-transition metal oxides: revision of the classical lone pair model. *Chem. Soc. Rev.* **2011**, 40, 4455.
- (53) Umari, P.; Mosconi, E.; De Angelis, F. Relativistic GW calculations on $\text{CH}_3\text{NH}_3\text{PbI}_3$ and $\text{CH}_3\text{NH}_3\text{SnI}_3$ Perovskites for Solar Cell Applications. *Sci. Rep.* **2014**, 4, 4467 DOI: 10.1038/srep04467.
- (54) Sarantopoulou, E.; Kollia, Z.; Cefalas, A. YF_3 : Nd^{3+} , Pr^{3+} , Gd^{3+} wide band gap crystals as optical materials for 157-nm photo-lithography. *Opt. Mater.* **2001**, 18, 23–26.
- (55) Li, K.; Xu, Z.; Xu, H.; Ryan, J. M. Semiconductive Coordination Networks from 2,3,6,7,10,11-Hexakis(alkylthio)-triphenylenes and Bismuth(III) Halides: Synthesis, Structure–Property Relations, and Solution Processing. *Chem. Mater.* **2005**, 17, 4426–4437.
- (56) Podraza, N. J.; Qiu, W.; Hinojosa, B. B.; Motyka, M. A.; Phillipot, S. R.; Baciak, J. E.; Trolier-McKinstry, S.; Nino, J. C. Band gap and structure of single crystal BiI_3 : Resolving discrepancies in literature. *J. Appl. Phys.* **2013**, 114, 033110.
- (57) Brown, I. D. What factors determine cation coordination numbers? *Acta Crystallogr., Sect. B: Struct. Sci.* **1988**, 44, 545–553.
- (58) Jaffe, A.; Lin, Y.; Beavers, C. M.; Voss, J.; Mao, W. L.; Karunadasa, H. I. High-Pressure Single-Crystal Structures of 3D Lead-Halide Hybrid Perovskites and Pressure Effects on their Electronic and Optical Properties. *ACS Cent. Sci.* **2016**, 2, 201–209.
- (59) Darnell, A. J.; McCollum, W. A. Phase diagrams of the bismuth trihalides at high pressure. *J. Phys. Chem.* **1968**, 72, 1327–1334.
- (60) Hsueh, H. C.; Chen, R. K.; Vass, H.; Clark, S. J.; Ackland, G. J.; Poon, W. C.-K.; Crain, J. Compression mechanisms in quasimolecular XI_3 ($\text{X} = \text{As}, \text{Sb}, \text{Bi}$) solids. *Phys. Rev. B: Condens. Matter Mater. Phys.* **1998**, 58, 14812–14822.
- (61) Devidas, T. R.; Chandra Shekar, N. V.; Sundar, C. S.; Chithaiah, P.; Sorb, Y. A.; Bhadram, V. S.; Chandrabhas, N.; Pal, K.; Waghmare, U. V.; Rao, C. N. R. Pressure-induced structural changes and insulator-metal transition in layered bismuth triiodide, BiI_3 : a combined experimental and theoretical study. *J. Phys.: Condens. Matter* **2014**, 26, 275502.
- (62) Zalkin, A.; Templeton, D. H. The Crystal Structures of YF_3 and Related Compounds. *J. Am. Chem. Soc.* **1953**, 75, 2453–2458.
- (63) Maguer, J.-J.; Crosnier-Lopez, M.; Courbion, G. Chimie Douce” Synthesis and ab Initio Structure Determination of $(\text{H}_3\text{O})\text{Yb}_3\text{F}_{10}\text{H}_2\text{O}$: Diamond Type Stacking of $\text{UOA}_{[8]}$. *J. Solid State Chem.* **1997**, 128, 42–51.